UC Irvine
UC Irvine Previously Published Works

Title

Three-dimensional reconstruction of cardiac flows based on multi-planar velocity fields

Permalink

https://escholarship.org/uc/item/2jq8n8dn

Journal

Experiments in Fluids, 55(11)

ISSN

0723-4864

Authors

Falahatpisheh, Ahmad
Pedrizzetti, Gianni
Kheradvar, Arash

Publication Date

2014-11-01

DOI

10.1007/s00348-014-1848-8

Peer reviewed

RESEARCH ARTICLE

Three-dimensional reconstruction of cardiac flows based on multi-planar velocity fields

Ahmad Falahatpisheh · Gianni Pedrizzetti · Arash Kheradvar

Abstract Measurement of the three-dimensional flow field inside the cardiac chambers has proven to be a challenging task. This is mainly due to the fact that generalized full-volume velocimetry techniques cannot be easily implemented to the heart chambers. In addition, the rapid pace of the events in the heart does not allow for accurate real-time flow measurements in 3D using imaging modalities such as magnetic resonance imaging, which neglects the transient variations of the flow due to averaging of the flow over multiple heartbeats. In order to overcome these current limitations, we introduce a multi-planar velocity reconstruction approach that can characterize 3D incompressible flows based on the reconstruction of 2D velocity fields. Here, two-dimensional, two-component velocity fields acquired on multiple perpendicular planes are reconstructed into a 3D velocity field through Kriging interpolation and by imposing the incompressibility constraint. Subsequently, the scattered experimental data are projected into a divergence-free vector field space using a fractional step approach. We validate the method in exemplary 3D flows, including the Hill's spherical vortex and a numerically simulated flow downstream of a 3D orifice. During the process of validation, different signal-to-noise ratios are introduced to the flow field, and the method's performance is assessed accordingly. The results show that as the signal-to-noise ratio decreases, the corrected velocity field significantly improves. The method is also applied to the experimental flow inside a mock model of the heart's right ventricle. Taking advantage of the periodicity of the flow, multiple 2D velocity fields in multiple perpendicular planes at different locations of the mock model are measured while being phase-locked for the 3D reconstruction. The results suggest the metamorphosis of the original transvalvular vortex, which forms downstream of the inlet valve during the early filling phase of the right ventricular model, into a streamline single-leg vortex extending toward the outlet.

A. Falahatpisheh · A. Kheradvar (✉)
Department of Mechanical and Aerospace Engineering,
University of California, Irvine, Irvine, CA 92697, USA
e-mail: arashkh@uci.edu

A. Falahatpisheh
e-mail: afalahat@uci.edu

A. Falahatpisheh · A. Kheradvar
Department of Biomedical Engineering,
University of California, Irvine, Irvine, CA 92697, USA

A. Falahatpisheh · A. Kheradvar
The Edwards Lifesciences Center for Advances Cardiovascular
Technologies, Henry Samueli School of Engineering,
University of California, Irvine, Irvine, CA 92617, USA

G. Pedrizzetti
Department of Engineering and Architecture,
University of Trieste, Piazzale Europa, 1, 34127 Trieste, Italy
e-mail: giannip@dica.units.it

1 Introduction

Certain blood flow patterns have been associated with changes in cardiac performance. For instance, different types of ventricular dysfunction have unique blood flow characteristics, and variations in blood flow patterns may indicate a change in overall cardiac performance. Quantifying the three-dimensional (3D) cardiac flow pattern has remained a challenging fluid dynamics problem, and

modern velocimetry techniques cannot yet acquire data with sufficient spatial and temporal resolution to considerably improve clinical diagnoses.

Currently, two-dimensional (2D) blood flow information—obtained by echocardiography—is beginning to be widely used to quantify cardiac dysfunction. While very useful, this information does not provide sufficient accuracy for characterizing complex three-dimensional flows, such as the flow in the right ventricle or in patients with congenital heart defects. Alternatively, flow-sensitive magnetic resonance imaging (MRI), 4D Flow MR, can provide flow information in 3D. However, 4D Flow MR cannot be applied to clinical routine. A further drawback of this technology is its averaging of the flow over hundreds of heartbeats, which neglects the transient variations in the flow. If the cycles are not perfectly periodic, as commonly happens in certain arrhythmias or cardiac conduction diseases, the image quality significantly degrades, and the resulting velocity fields may not be reliable (Asakawa et al. 2003).

Echocardiographic techniques based on particle image velocimetry (PIV) or color-Doppler have been recently employed by a number of research groups (Kim et al. 2004; Hong et al. 2008; Kheradvar et al. 2010; Westerdale et al. 2011; Zhang et al. 2011; Cimino et al. 2012) and are capable of evaluating the instantaneous vortical blood motion in the cardiovascular system. The PIV-based methods, known as Echo-PIV, permit high-frequency acquisition during a single beat in 2D. Since current Echo-PIV methods are limited to two-dimensional visualization (the scan-plane), they provide an incomplete picture of three-dimensional flow structures.

Similar to 2D Echo-PIV, it was anticipated that the recent advances in 3D echocardiography would provide further opportunities for 3D mapping of cardiac flow with reasonable accuracy (Sengupta et al. 2012). Recently, the flow in a curved tube was reconstructed three-dimensionally using a few parallel planes of ultrasound PIV (Poelma et al. 2011). However, this technique is limited to flows whose velocity component is mainly along one direction.

The current 3D echocardiography does not provide a framework to implement conventional PIV techniques with an acceptable temporal and spatial resolution. This is mainly due to the limited frame rate of 3D echocardiographic acquisitions, a limitation related to the computational requirements of parallel processing of large datasets of ultrasound RF data, in addition to the fixed speed of ultrasound waves. Substantial technological advancement will be required to overcome these limitations.

Ziskin et al. (2011) introduced a method in which 2D cross-correlation on multiple planes along different directions was used for obtaining 3D velocity field. They used multiple cameras to create perspective images in order to reconstruct velocity field in 3D, which is done by mapping

functions during a pre-experiment calibration. Here, we introduce a different approach to reconstruct the 3D flow field based on multi-planar particle image velocimetry (MPPIV), abbreviated as MPPIV, that requires imposing the incompressibility constraint to the flow using a fractional step approach. By taking advantage of the physical constraint given by incompressibility that relates different velocity components, a consistent 3D vector field can be generated.

In the present work, we describe the overall MPPIV concept and its specific mathematical implementation in Sect. 2. The systematic validations, performed to compare the reconstructed flow fields with known 3D velocity fields, are provided in Sect. 3. An exemplary application for quantification of the flow inside a mock model of the right ventricle is presented in Sect. 4 whereby taking the advantage of the periodicity of the cardiac cycle, 2D velocity fields from multiple perpendicular planes in different locations are obtained in different heartbeats (phase-locked) and reconstructed in three dimensions by MPPIV. The results are summarized in Sect. 7.

2 Methods

The method is composed of three sequential processes: (1) two-dimensional (2D) two-component (2C) velocimetry on predefined planes; (2) interpolation in 3D space; and (3) enforcing the incompressibility constraint. Each individual process is described here in sequence.

2.1 2D–2C velocimetry

The first step of multi-planar velocimetry is the acquisition of two-dimensional velocity fields on two perpendicular stacks using available acquisition modalities (PIV, Echo-PIV). Each stack should be composed of parallel 2D velocity field slices with the inter-slice distance representing the resolved length scale. We considered the stacks parallel to rectangular Cartesian coordinates with each slice in a stack containing only two in-plane components of velocity.

In this study, different slices of the stack were images acquired by a single high-speed camera (Y3, IDTVision, Inc.), which in principal can be replaced by a matrix array ultrasound transducer. The velocity values associated with the measurement points (typically a grid) were obtained using PIV methods. A single camera was used for acquiring different slices of the stack in sequence by taking advantage of the periodicity of the flow. The accuracy of the analysis, when using one camera, depends on the effective periodicity of the flow field in addition to the precision of the velocimetry itself. In the case of a multi-slice acquisition source (e.g., a matrix array ultrasound transducer for multi-planar Echo-PIV), 2D velocity fields would be acquired simultaneously on each slice in the stacks.

2.2 Interpolation

Kriging interpolation has been found to be a useful method for the reconstruction, interpolation, and smoothing of 2D and 3D experimental data (Gunes and Rist 2007, 2008). In addition, Kriging is ideal for sufficiently high-resolution experimental data (Gunes and Rist 2007). It was shown that both DNS-based and Kriging procedures can effectively eliminate the background noise and measurement errors in experimental data (Gunes and Rist 2007). However, in many cases, DNS-based interpolations are not available and an alternative is needed when the resolution is not sufficiently high.

To assemble the slices of 2D–2C velocity fields into a 3D vector field, we used the Kriging interpolation method (Cressie 1992), which can interpolate scattered data into a regular Cartesian staggered 3D grid. Kriging is an optimal interpolation technique based on regression against the observed values, $Z(\mathbf{x}_\alpha)$, of neighboring data points $\mathbf{x}_\alpha$, which are weighted according to the spatial covariance values. Compared to other interpolation methods, in Kriging, the weights are assigned according to a moderately data-driven weighting function, rather than an arbitrary function. The Kriging method compensates for the clustering (proximity) effect that is often seen in other interpolation techniques, such as the inverse distance square estimate, which causes a bulls-eye effect (Cressie 1992). This can happen near the intersection of the slices that belong to different stacks. The Kriging method assigns less weight to individual points within a cluster than to isolated data points. Therefore, clusters are treated more like single points.

The method offers estimation error or "Kriging variance" along with the estimate of the variable, $Z(\mathbf{x})$; this estimation error provides a basis for stochastic simulation of the possible realizations of Z as

$$Z^*(\mathbf{x}) - m(\mathbf{x}) = \sum_{\alpha=1}^{n(\mathbf{x})} \eta_\alpha [Z(\mathbf{x}_\alpha) - m(\mathbf{x}_\alpha)] \tag{1}$$

where $\mathbf{x}_\alpha$ and $\mathbf{x}$ are the location vectors for the neighboring data points (indexed by α), and the estimation point, respectively. $n(\mathbf{x})$ is the number of data points in the local neighborhood used for the estimation of $Z^*(\mathbf{x})$. For this study, we used the eight nearest points. $m(\mathbf{x})$ and $m(\mathbf{x}_\alpha)$ are expected values of $Z^*(\mathbf{x})$ and $Z(\mathbf{x}_\alpha)$, respectively. $\eta_\alpha(\mathbf{x})$ is the Kriging weight assigned to $Z(\mathbf{x}_\alpha)$ for estimation location $\mathbf{x}$. A neighbor receives different weights when used for different estimation locations. $Z(\mathbf{x})$ is treated as a random field with a trend component, $m(\mathbf{x})$, and a residual component, $R(\mathbf{x}) = Z(\mathbf{x}) - m(\mathbf{x})$. Kriging estimates the residual at $\mathbf{x}$ as a weighted sum of residuals at surrounding data points. Kriging weights, η_α, are derived from the covariance function or semivariogram, which characterizes a residual component. Distinction between trend and residual is somewhat arbitrary and varies with scale. We used the spherical semivariogram model of

$$\gamma_z(h) = \begin{cases} \frac{3}{2}\frac{h}{a_0} - \frac{1}{2}\left(\frac{h}{a_0}\right)^3 & \text{if } h \leq a_0. \\ 1 & \text{if } h > a_0, \end{cases} \tag{2}$$

where h is the distance of the estimate point from each neighboring point, and a_0 is selected as the mean of the distances.

A 3D Cartesian staggered grid was generated with face-centered normal velocity components, which facilitates achieving a second-order accuracy for the calculation of flux balance on each cell, as explained in Sect. 2.3. A typical cell in the grid is shown in Fig. 1. The grid was created such that it covered the stacks. Kriging interpolation was separately implemented on the u-, v-, and w-components of the velocity. Since slices in the two perpendicular stacks contain different velocity components, the neighboring points for each estimation point, $\mathbf{x}$, in the interpolation of different velocity components can be different. In other words, the interpolation identified for the eight nearest velocity components available in the nearby slices, which may belong to different stacks.

2.3 Constraint of incompressibility

Interpolation methods have been widely used for the reconstruction of 3D flows. Recently, phase-averaged velocities were shown to be obtainable from spatial interpolation of two perpendicular stacks of parallel planes whose in-plane velocity fields were measured by 2D PIV (Stamatopoulos et al. 2011). Others have shown that by using synchronized PIV and infrared thermography measurements, flow field in three dimensions can be reconstructed (Harlander et al. 2012). In their work, Harlander et al. used a mesh-free reconstruction method based on radial basis functions. Time-resolved PIV in two orthogonal stacks of planes and linear interpolation was then utilized to find the three-dimensional phase-averaged data (Sung and Yoo 2001).

In principle, the interpolated velocity field does not necessarily satisfy the incompressibility condition of the flow in 3D. Therefore, as a first requirement for producing a divergence-free velocity field, the field must be modified accordingly. There are different approaches in imposing the continuity equation. Su et al. utilized the concept of minimization of errors for the interpolation of 3D velocity data on the basis of the continuity constraint (Su and Dahm 1996; Liburdy and Young 1992). They inserted the continuity constraint into the local minimization functional of the interpolation procedure—a functional composed of several terms including the local measurements and smoothness requirement. In such an approach, incompressibility is one
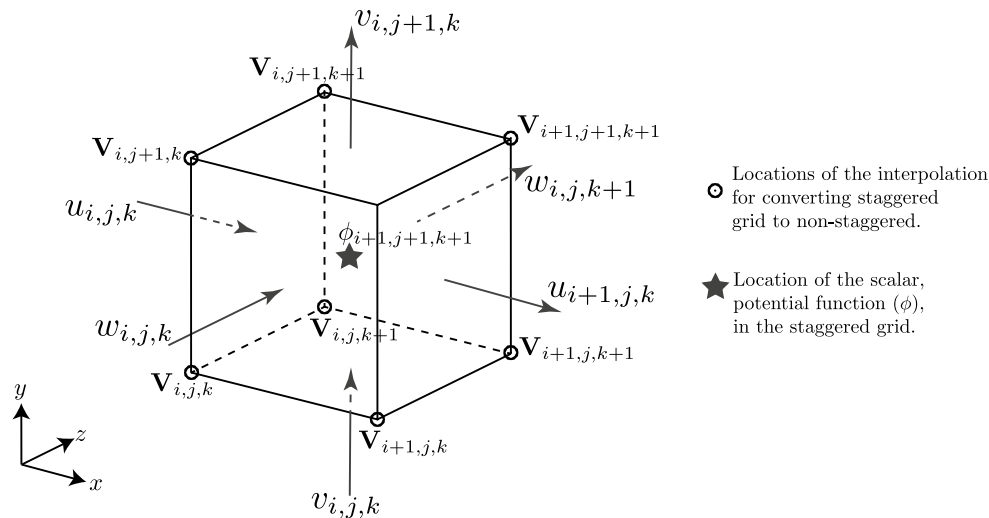
Fig. 1 Indexing and locations of velocity components, and divergence of the velocity for a typical cell in the staggered grid

of the local weighting factors that is not exactly satisfied. Continuity has also been used to estimate the accuracy of 3D (dual-plane and stereo) PIV measurements (Mullin and Dahm 2005, 2006).

Afanasyev and Demirov (2005) employed incompressibility in planar PIV measurements in a filtering procedure to improve the quality of data. Their concept is based on the fact that the 2D velocity field can be decomposed into a non-divergent component and a relatively small divergent component. Another approach is the interpolation of a continuous velocity field from sparse information based on local kernels, including methods based on sparse measurements (Zhong et al. 1991; Zhong 1995; Vedula and Adrian 2005), as well as those based on Lagrangian numerical methods (Novikov 1983; Leonard 1985). In this case, the individual kernels are directly solenoidal and ensure the continuity of the resulting field. This approach needs some care in the interpolation process because the kernel size must be locally adapted to the density of the available information. Furthermore, this typically requires vector information as an input. However, this method has not yet been employed to reconstruct a 3D field from 2D information similar to our present work. Another interesting approach has been recently applied for metrological applications in estimating the vertical component of the velocity (Ratto et al. 1994; Núñez et al. 2006, 2007). In this approach, the vertical velocity is reconstructed on the basis of a known horizontal velocity and a given boundary condition. In this method, a proper weight of the incompressible correction is used and then this weight is optimized for a specific application. Here, we follow a similar approach, in that we impose the continuity constraint on arbitrary velocity data, either in position or in the number of components. Next, optimization weights are replaced by

the concept that continuity must be satisfied exactly, which is achieved by correcting the velocity field using an irrotational field. In fact, we follow the approach developed for the fractional step method in computational fluid dynamics, and the interpolated velocity field is projected into a divergence-free subspace (Kim and Moin 1985). This can be achieved by adding an irrotational velocity field whose divergence cancels out the divergence of the interpolated velocity. This creates a divergence-free velocity field that adjusts the interpolated flow field, satisfies the continuity of the flow, and eliminates any sink/source in the domain that may result from 2C velocimetry.

This correction provides a physical consistency to the velocity field and can also be particularly important when computing additional quantities derived by velocity gradients, which intrinsically incorporate the zero-divergence condition.

The projection is carried out according to

$$\mathbf{u} = \mathbf{u}_{\text{int}} + \mathbf{u}_{\text{corr}}, \tag{3}$$

where $\mathbf{u}$ is the *divergence-free interpolated velocity field*, $\mathbf{u}_{\text{int}}$ is the Kriging interpolated field, here referred to as the *simply interpolated velocity field*, and $\mathbf{u}_{\text{corr}}$ is the velocity correction expressed as the gradient of a potential function ϕ

$$\mathbf{u}_{\text{corr}} = \nabla \phi. \tag{4}$$

Combining the two sets of orthogonal planes doubles the information available. In particular, it provides three components of the velocity vector and allows for an improved estimate of the vorticity field. The correction is an irrotational field that can only adjust the divergence without affecting the vorticity field. Moreover, when using just parallel slices, one velocity component has to be completely
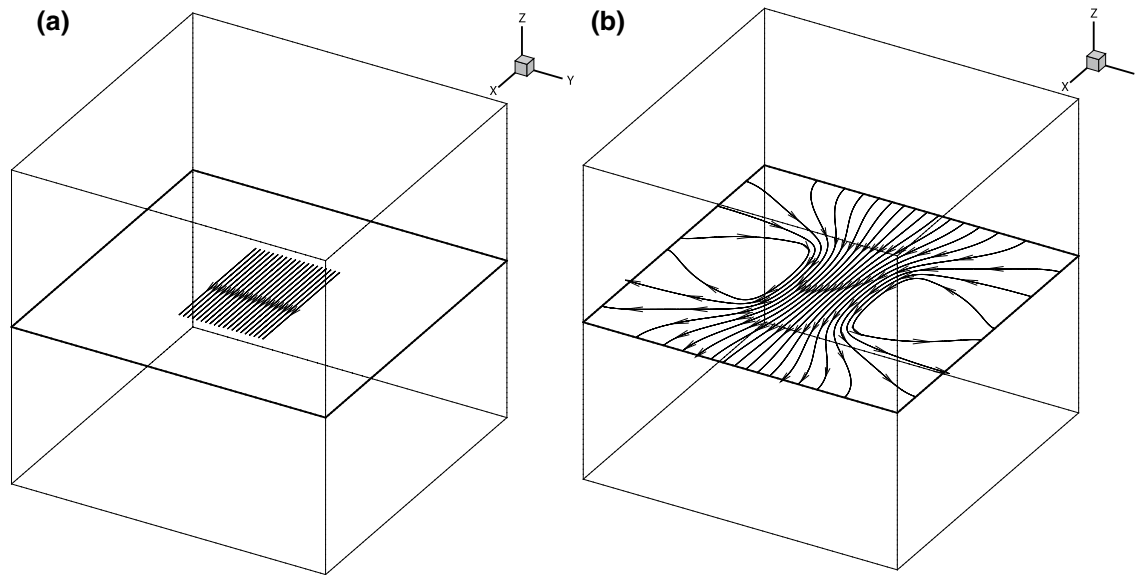
Fig. 2 Concept of imposing incompressibility is illustrated here. **a** Streamlines for an interpolated field at $z = 0$ plane. It can be observed that streamlines disappear spontaneously; **b** streamlines at $z = 0$

plane of the same interpolated field shown at (**a**) once the incompressibility constraint is imposed to the velocity field to make it divergence-free

reconstructed and the mean flow components cannot be found.

Application of the divergence-free constraint, $\nabla \cdot \mathbf{u} = 0$, to Eq. (3) results in the Poisson equation for the potential

$$\nabla^2 \phi = -\nabla \cdot \mathbf{u}_{\text{int}}, \tag{5}$$

where $\nabla \cdot \mathbf{u}_{\text{int}}$ is the divergence of the interpolated velocity. We did not consider any rigid wall at the end of the integration domain, and typically, we do not have the walls' coordinates (and their velocity) in these problems. Thus, the Neumann condition was not considered the most appropriate choice. Therefore, Dirichlet boundary conditions, with zero values on all six boundary faces of the domain, were employed for ϕ in (5); physically, this ensures that no (arbitrary) net flow is introduced by the correction. Alternatively, the Neumann condition can be applied to all six end faces, which give no net flow as well; however, this implies a zero velocity at the end faces, which appears to be a more severe constraint than the zero mean flow.

Numerically, the potential ϕ was defined at the cell center of the staggered grid, and the Poisson equation (5) was satisfied therein. The right-hand side and the Laplacian operator were estimated based on the second-order accurate finite difference at the cell center and the gradient components in (4) at the face center of the staggered grid. Calculations were implemented in C++ and using Poisson Library from Intel® MKL 10.3.

It should be mentioned that once a scale is resolved, there is no difference between small and large scales because correction is found based on the solution of a

linear problem in which scales are solved separately. The presence of different resolutions can be an issue and is discussed in the limitation section.

2.3.1 Illustration of the incompressibility constraint

The importance of imposing the solenoidal condition to the interpolated velocity field can be highlighted by examining a cubic domain in which there is only a uniform flow along the x-direction in the vicinity of the cube's centroid. The interpolated velocity field in the $z = 0$ plane is shown in Fig. 2a. The original flow was laterally surrounded by a shear layer with a sharp divergence at both ends. The 3D divergence-free interpolated velocity, which was constrained not to introduce any net volumetric flow, is shown in Fig. 2b. The divergence-free interpolated flow preserves the same vorticity field and imposes fluid continuity. Throughout this study, streamlines were generated using the Tecplot® visualization package (Amtec Engineering, Bellevue, WA). Tecplot uses a two-step, second-order Runge–Kutta method to compute the streamlines. We utilized both forward and backward integrations from the starting points to calculate the streamlines.

3 Validation of the technique in test cases

We systematically verified the behavior of the reconstruction algorithm. For this purpose, we employed two benchmarks in which the 3D divergence-free interpolated fields

were compared with known flow fields having vortex features: first, a Hill spherical vortex (HSV) (Hill 1894), and second, a 3D DNS flow field behind a slender orifice (Domenichini 2011). Here, we refer to these velocity fields as true solutions.

The 3D flow fields of these two benchmark flows were sampled in two perpendicular stacks, *xy*- and *yz*-stacks, which are referred to in this section as the 2*C-velocimetry sampled data*. On each slice, the out-of-plane component of velocity was disregarded. These sampled data were generated for four different stacks with different numbers of samples. In all the stacks, each slice contained 32×32 samples, which were uniformly distributed. Increasing the slice resolution adds more information to the original data to which the interpolation and correction will be applied. In other words, if the slice has a higher resolution which can be achieved by using different seeding or different optical magnification, the accuracy of 2C velocimetry, in terms of the number of the resulted velocity vectors, is higher. Therefore, the uncertainty in the experimental data is reduced, which results in a more accurate 3D interpolated velocity field and, consequently, a more accurate divergence-free interpolated velocity field. We increased the number of slices in each stack from 4, 8, 16, to 32. In each stack, the distance between the slices was kept the same, which created a uniform stack. Furthermore, to mimic the uncertainty associated with experimentally acquired velocity measurements, different levels of noise were introduced to the 2C-velocimetry sampled data starting from a field with no noise, then adding 15 and 30 % Gaussian noise, relative to the 3D field velocity scale. Therefore, for each benchmark flow field, a total of 12 2C-velocimetry sampled datasets were generated. The purpose of Gaussian noise was to artificially create uncertainty in the velocity field of each slice to test the performance of our technique. This uncertainly might come from different sources including PIV postprocessing procedures, errors related to the experimental setup, or three-dimensionality in the slice (i.e., particles going into or out of the light sheet).

In all the tests cases, the 3D divergence-free interpolated velocity fields were obtained with a resolution of 64^3 and compared with the true solution at the same points. The root mean square (RMS) error, reported here as a function of the number of slices in the stack, statistically represents the difference between either the simply interpolated or the divergence-free interpolated velocity field and the true solution

$$\text{Err}_{\text{RMS}i} = \frac{\sqrt{\frac{1}{n} \sum \left[(u_T - u_i)^2 + (v_T - v_i)^2 + (w_T - w_i)^2 \right]}}{\text{Velocity Scale}},$$

(6)

where $n = 64^3$ is the resolution of the three-dimensional domain, subscript T stands for true velocity field, and

subscript i can be either the simply interpolated or divergence-free interpolated velocity field. Here, we tested the hypothesis that the RMS error would be reduced in a divergence-corrected field as compared to the simply interpolated field.

3.1 Test case 1: Hill spherical vortex

The HSV is a convenient example for the purpose of validation (Hill 1894). This vortex is an extreme member of the Norbury family of vortex rings, (Norbury 1973) and is used as a model in applications such as the motion of bubbles and droplets at a high Reynolds number. The vorticity inside the HSV varies linearly with the distance from the axis of symmetry. In a HSV, the external flow is irrotational around a sphere, whereas the internal flow has an axisymmetric vorticity distribution. The spherical symmetry of the HSV vector field challenges our algorithm, which is based on a Cartesian grid.

A HSV is specified by the Stokes (axisymmetric) streamfunction as

$$\psi = \begin{cases} \frac{3}{4} V r^2 \left(1 + \frac{\rho^2}{R^2} \right) & \rho^2 \leq R^2 \text{ (internal flow)} \\ \frac{3}{4} V r^2 \left(\frac{R^3}{\rho^3} - 1 \right) & \rho^2 \geq R^2 \text{ (external flow)} \end{cases}$$

(7)

where R specifies the size of the spherical vortex, V is the external uniform vertical velocity taken as the velocity scale in Eq. (6); $r = \sqrt{x^2 + y^2}$ and $\rho = \sqrt{r^2 + z^2}$ are the cylindrical and spherical radial coordinates, respectively. The velocity field in Cartesian coordinates is computed by the streamfunction as

$$u = -\frac{x}{r^2} \frac{\partial \psi}{\partial z}; \quad v = -\frac{y}{r^2} \frac{\partial \psi}{\partial z}; \quad w = \frac{1}{r} \frac{\partial \psi}{\partial r}$$

(8)

We created a HSV with unit radius and velocity scale in a cube of size $1.5 \times 1.5 \times 1.5$. Figure 3 shows the RMS error for the simply interpolated and divergence-free interpolated velocity fields; in all the cases, the divergence-free interpolated velocity field showed an improvement with respect to the simply interpolated field. When no noise was introduced in the 2C-velocimetry sampled data, the RMS error was not significantly reduced by applying the incompressibility constraint, mainly because the sampled velocity field was already divergence-free, thus providing an indirect validation of the interpolation procedure. However, as the level of noise increased, the divergence correction adjusted the interpolated flow field more significantly toward reducing the difference in RMS error. In other words, the greater the level of uncertainty in the velocimetry data, the greater the benefit of ensuring the incompressibility constraint. Figure 4 depicts the result obtained for the 3D divergence-free interpolated

Fig. 3 RMS error for the simply interpolated and divergence-free interpolated velocity fields versus the number of slices in Hill's spherical vortex. *Black*, *blue*, and *red* represent 0, 15, and 30 % Gaussian noise in the 2C-velocimetry sampled data, respectively. The stacks for 2C-velocimetry sampled data possess 4, 8, 16, and 32 *xy*- and *yz*-slices at 32×32 resolution
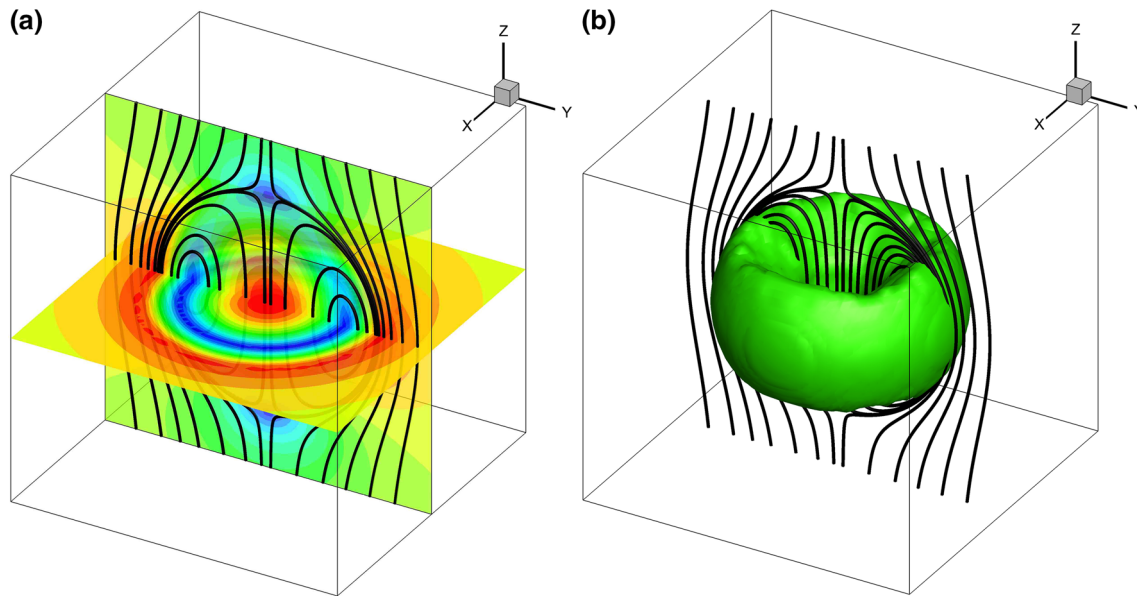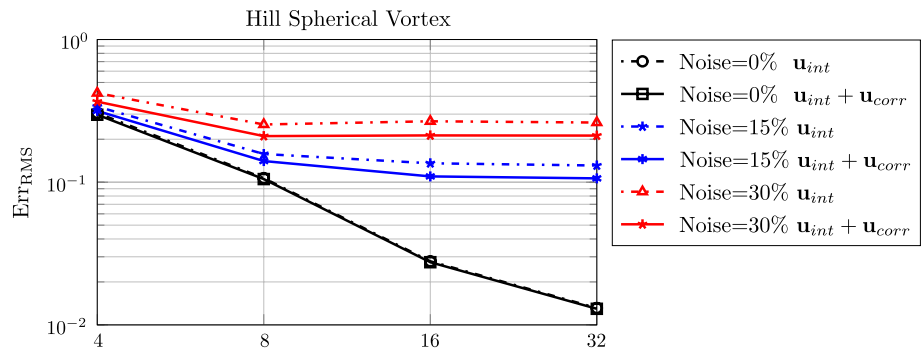

Fig. 4 Divergence-free interpolated velocity field for a Hill's spherical vortex. Velocity magnitude along with streamlines is shown in **a** and **b** isosurface of $\lambda_2 = -2.0$ (Jeong and Hussain 1995)

velocity field by using 32 slices for each stack in the 2C-velocimetry sampled data (no noise). The spherical symmetry can be observed in Fig. 4b where the vortex ring is illustrated by the isosurface of λ_2 (Jeong and Hussain 1995).

3.2 Test case 2: 3D flow behind slender orifice

For the second benchmark, we used the 3D velocity field behind a slender orifice, which was previously investigated numerically (Domenichini 2011). In that study, the three-dimensional vortex formation due to the impulsively started flow through slender openings was numerically simulated. The orifice was formulated as two half-circles connected by straight segments as shown in Fig. 5. We used the numerical data for a length-to-width ratio of 4 at $t = 10$, as shown in Fig. 5 (Domenichini 2011).

In this test case, the velocity scale in Eq. 6 was taken as the square root of the mean kinetic energy normalized by the density. In agreement with the previous findings for the HSV, the results demonstrate that imposing the incompressibility constraint improves the accuracy of the flow field, and this improvement is more prominent with decreasing levels of signal-to-noise ratio, as evidenced in Fig. 6a.

To provide further insight into the quality of the Kriging interpolation, we examined the effect of using alternating half-planes in *xy*- and *yz*-stacks instead of full planes on Err_{RMS}, as shown in Fig. 7. This made the 2C-velocimetry sampled data even more sparse. In this arrangement, half of the slices in each stack were in one side of the domain's centroid and the rest were on the other side. Figure 6b illustrates the result of employing alternating half-planes as 2C-velocimetry sampled data. Although there was a slight increase in the calculated Err_{RMS} of alternating half-plane
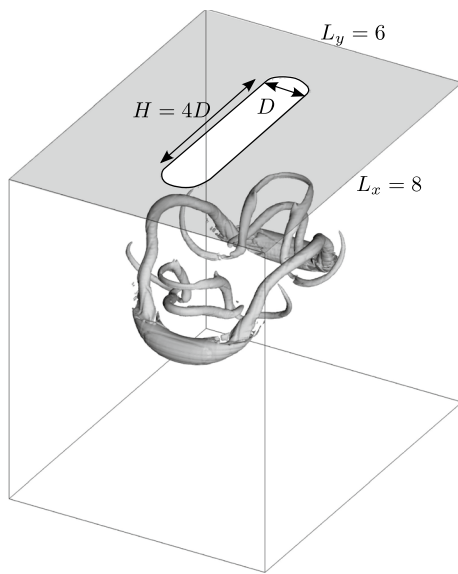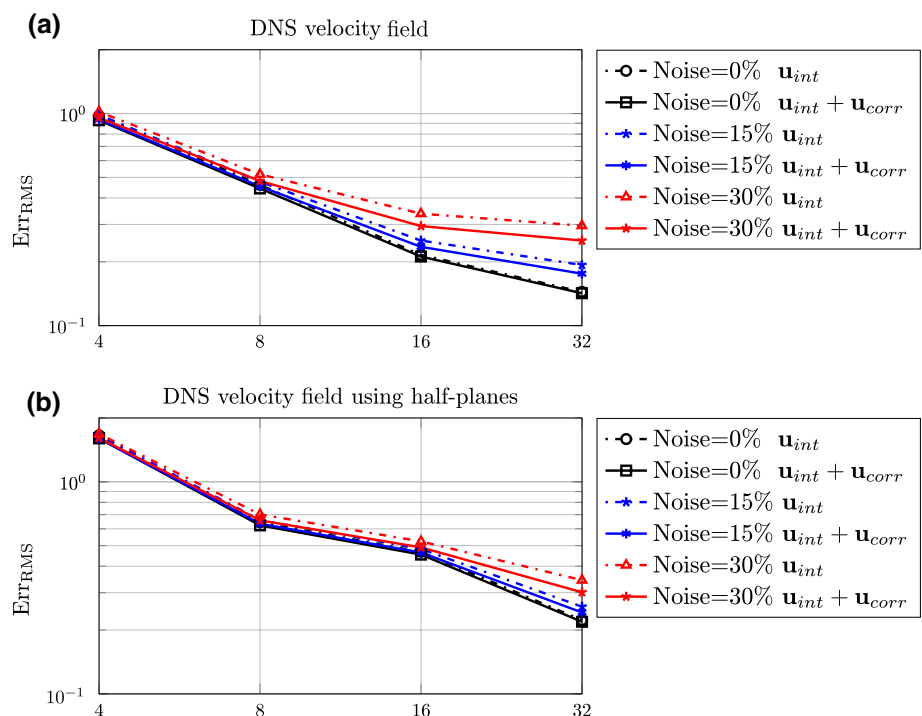
Fig. 5 Result of the direct numerical simulation of a three-dimensional vortex formation through a slender opening (Domenichini 2011). The geometry of the orifice and the horizontal section of the computational box are illustrated in the figure. The vortex is visualized for the isosurface of $\lambda_2 = -5$ at $t = 10$

data, the results were consistent with the full-plane case. It indicated that the need for more planes to fully resolve the underlying three-dimensional flow is not critical when the MPPIV method is employed. This emphasized the robustness of the approach and the expected improvement with increasing information.

4 Application to experimental flow in a model of the right ventricle

The right ventricle (RV) is the crescent-shaped chamber of the heart, which pumps venous blood flow for oxygenation to the lungs. This chamber is smaller than the left ventricle (LV) and is more compliant. To date, flow inside the LV has been extensively investigated in vitro and in vivo. However, very little quantitative information is available on flow patterns inside the RV. The particular reasons for this lack of knowledge include (1) the non-symmetric, crescent shape of the RV, which is wrapped around the LV and limits 2D echocardiographic flow evaluations; and (2) highly time-dependent RV flow that significantly reduces the accuracy of the studies performed by MRI. Overall, the study of the RV is a relatively young field. Recently, the flow of a patient-specific RV model reconstructed from echocardiography images was numerically assessed, and evidence for the presence of a complex three-dimensional flow pattern was observed (Mangual et al. 2012). Furthermore, the blood flow in the RV of healthy adults was experimentally measured by using 4D Flow MRI (Fredriksson et al. 2011). Also, the performance of the RV was compared with the LV, demonstrating the presence of a more direct route from the inlet to the outlet (Fredriksson et al. 2011).

Here, we test the method described in Sect. 2 to verify the feasibility of the MPPIV method in an actual experimental setting. This test case provides experimental observations of the flow inside a model of the right ventricle, for the first time.

Fig. 6 RMS error for the simply interpolated and divergence-free interpolated velocity fields versus the number of slices with Domenichini's DNS velocity field taken as the true solution. *Black*, *blue*, and *red* represent 0, 15, and 30 % Gaussian noise in the 2C-velocimetry sampled data, respectively. The stacks for 2C-velocimetry sampled data possess 4, 8, 16, and 32 xy- and yz-slices at 32×32 resolution. **a** RMS error of using full planes and **b** result of using alternating half-planes
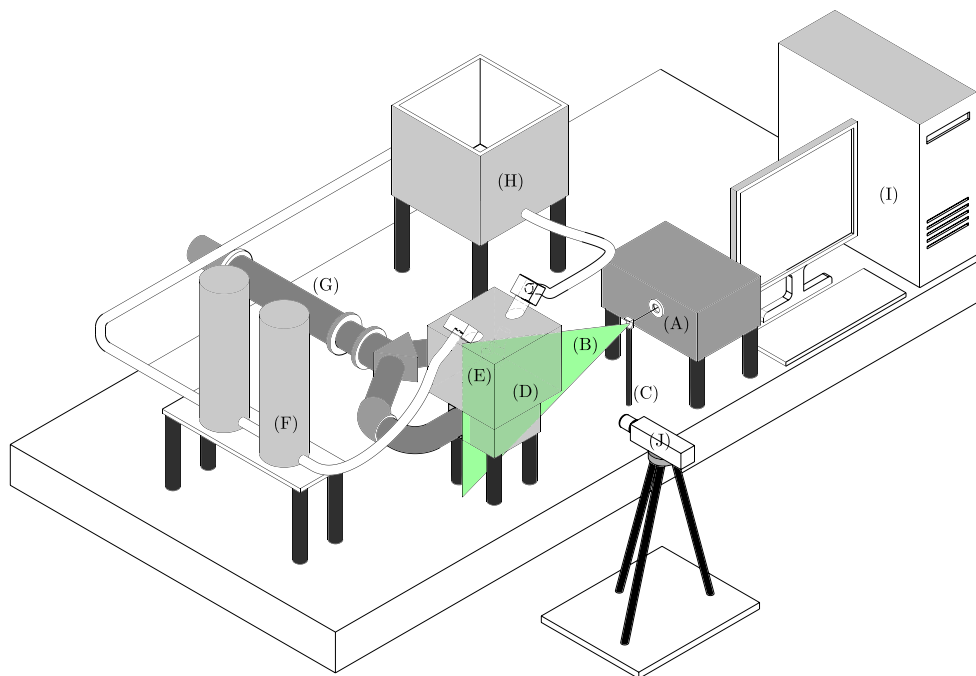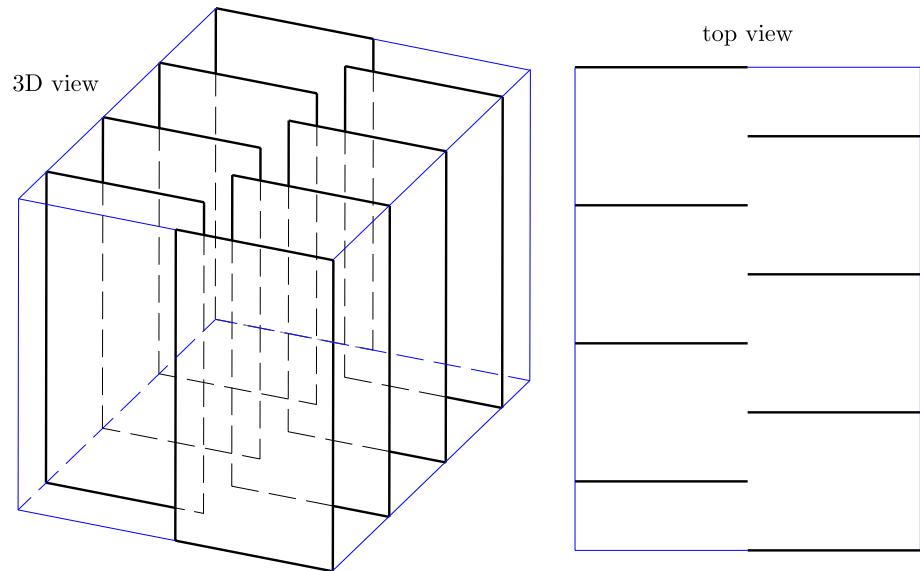
Fig. 8 Schematic of the pulsatile heart-flow simulator. *a* Nd:YLF green pump laser; *b* laser light sheet for the illumination of the micro-fluorescent particles inside the model of the right ventricle; *c* cylindrical lens for converting laser beam to laser sheet; *d* box filled with water containing the right ventricle model; *e* right ventricle model immersed in *d; f* resistance chambers for adjusting the systemic venous and right atrial pressures in the RV model; *g* positive displacement pump for creating pulsatile flow in the RV model; *h* open-to-atmosphere lung reservoir; *i* computer and data acquisition system; *j* high-speed camera

4.1 Experimental setup

We used a heart-flow simulator consisting of a hydraulic pump system (Superpump system, VSI, SPS3891, Vivitro systems Inc., Victoria, BC, Canada) that operates based on a VSI Wave Generator VG2001 (Vivitro Systems Incorporated, Victoria, BC, Canada), as previously described

(shown in Fig. 8) (Falahatpisheh and Kheradvar 2012). The system is comprised of a silicone RV sac with adult human dimensions suspended in a pressurized container. The thickness of the sac is 1.0 mm. The sac is a patient-specific RV model reconstructed from echocardiography. The periodic, pulsatile flow in the circulatory system was generated by the response of the ventricular sac to the input
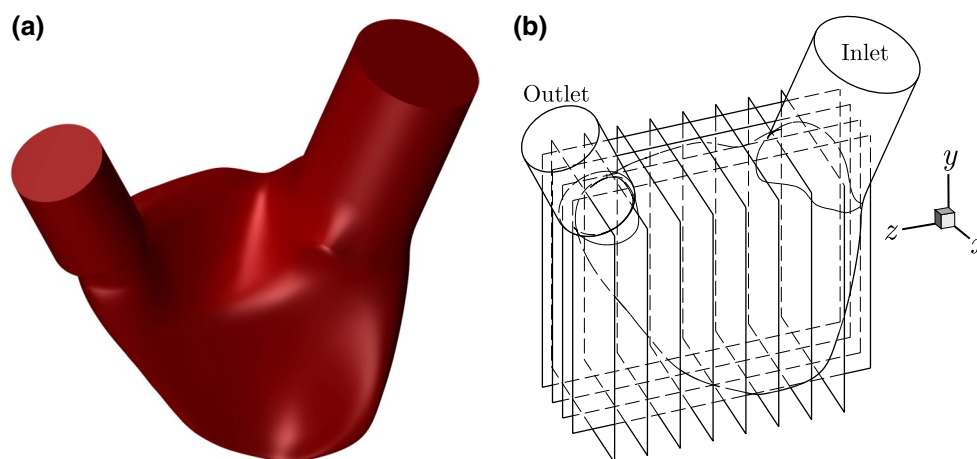
(a)

(b)

Fig. 9 RV model and the stacks configuration in PIV experiment. **a** Cast of the RV used to manufacture the silicone rubber model. The geometry of the RV model is acquired from echocardiography data.

b Schematic of the two perpendicular stacks used for 3D reconstruction of the RV velocity field

waveforms provided by the pump, and the two bioprosthetic heart valves at tricuspid (inlet) and pulmonary (outlet) valve positions. We used 27- and 21-mm heart valves (St. Jude Medical, Little Canada, Minnesota) for the inlet and outlet valves, respectively. Physiological waveforms, at a frequency of 60 beats per minute, were created by a wave generator (VG2001). Particle-seeded water was used as the circulating fluid (Kheradvar and Gharib 2009). Neutrally buoyant, orange fluorescent particles with diameters in the range of 60–80 μm were used to seed the flow. A high-speed digital camera was used (1,000 frames per second, 1,280 × 1,024; Y3, IDTVision, Inc., Pasadena, CA) whose optical axis was placed perpendicular to the illuminated laser sheet to capture the image sequence of the particle fields. The pair of images was taken from the planes of interest, in which the fluorescent particles were illuminated by a Nd:YLF green pump laser (Evolution 30, Coherent, Inc., Santa Clara, CA) with pulse separation of 1 millisecond. The laser sheet thickness was 1.5 mm. No combination of multiple cycles was made in obtaining the 2D velocity frames.

PIV was performed using PIVview2C (PIV TEC Gmbh, Göttingen, Germany). An interrogation window of 32 × 32 pixels with 50 % overlapping, multi-grid interrogation algorithm, 3-Point Gauss Fit (Willert and Gharib 1991) for peak detection, normalized median filter equal to 3.0 for validation, and median filtering with a kernel size of 3 × 3 were used. Data were smoothed using a Gaussian-weighted kernel of width 1. Standard calibration was performed by measuring the diameter of the inlet tube at the position of laser sheet. In the particle images, the number pixels on the diameter of the tube were counted and converted to the physical length based on the measured tube diameter.

4.2 MPPIV performance

We reconstructed the 3D velocity field inside the RV model using our MPPIV method. The geometry of the RV model in the pumping phase is shown in Fig. 9a. By 2C velocimetry, we acquired the planar velocity fields from two perpendicular stacks including a total of 12 slices encompassing the entire RV chamber at 1,000 frames per second (fps), as shown in Fig. 9b. It should be noted that the heart-flow simulator allowed us to rotate the RV model while keeping the position of the camera intact. In other words, the default camera view was set to image the stack of yz-planes (Fig. 9b), and by rotating the RV model 90°, the camera could capture the stack of xy-planes, as can be seen from Fig. 10. The stacks consisted of eight xy-slices for the larger dimension and four yz-slices for the smaller dimension of the RV. The planes were perpendicular within ±5° at their intersection. The results of the 2C-PIV for two selected planes are shown in Fig. 10. The data were acquired from multiple cycles taking the advantage of periodicity of the flow and were phase-locked for three-dimensional reconstruction. Care was taken to have a perfect similarity between experiments in multiple planes. We acquired the velocity field in each slice separately and in sequence with a single camera. Two supplementary videos show the 2D velocity fields, which are obtained by 2C-PIV, in two selected planes from the xy- and yz-stacks. Video 1 shows a yz-plane and video 2 illustrates an xy-plane. In video 1, the inlet valve is located on the left and the outlet valve is on the right. In video 2, the visible valve is the outlet valve and the inlet valve is behind the laser sheet. The resolution of the velocity field obtained by 2C-PIV in each slice was 79 × 63. To reconstruct the flow in 3D, a domain
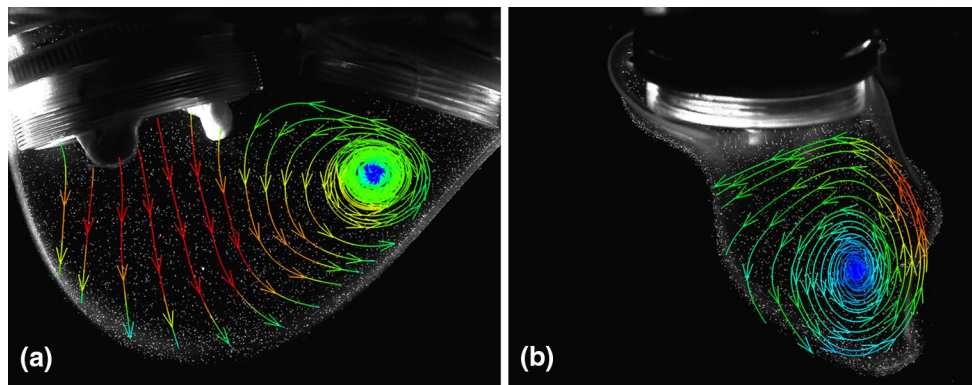
Fig. 10 Streamlines obtained from 2C-PIV in the RV model. Two perpendicular views are shown. **a** Streamline for one of the planes parallel to yz-plane at $t = 262$ ms. **b** One of the slices parallel to xy-plane at $t = 12$ ms
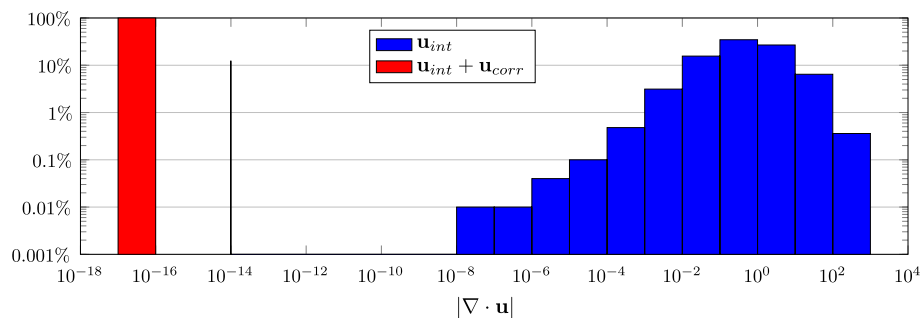

Fig. 11 Histogram for the absolute value of divergence of the interpolated velocity field normalized by the total number of the grids inside the RV model. The total number of grids inside the RV model was 220,272. *Bins without any bars* represent zero counts. The *line* on 10^{-14} belongs to the case of the simply interpolated velocity field

and represents all the grids whose absolute velocity divergence is less than 10^{-14}. For the divergence-free field, all of the 220,272 grids exhibited an absolute divergence value less than 10^{-16} as shown by the *red bar*

including the RV, with the dimensions of $10 \times 7.2 \times 8$ cm^3 at a velocity vector resolution of $64 \times 64 \times 64$, was used for interpolation. Both of the orthogonal stacks were used for interpolation.

The histogram of the divergence of the simply interpolated velocity is shown in Fig. 11. Out of 64^3 grid points, 220,272 points inside the RV model were considered for analysis. According to the histogram in Fig. 11, the majority of the flow field initially exhibited a non-physical divergence; therefore, the incompressibility correction (numerically $|\nabla \cdot \mathbf{u}| < 10^{-16}$) represents an important step in the creation of a 3D velocity vector field. This can also be recognized by studying the flow streamlines that were found to be mostly continuous in the divergence-free interpolated field, whereas in the simply interpolated field they were shorter and disconnected. To quantitatively verify this, 4,913 streamlines were generated inside the RV model. We calculated the streamline's length and normalized it by the maximum streamline length in the divergence-free velocity field. Figure 12 shows the histogram of the length

difference between streamlines, originating from the same points, in the divergence-free interpolated and the simply interpolated velocity fields. It is evident that the length of streamlines increased after imposing the incompressibility constraint, supporting the previous observation (Fredriksson et al. 2011) of a streamlined flow with a moderate circulation behind the inflow region. Figure 13 shows a few sample streamlines to support the physical interpretation of the result.

4.3 Results related to RV vortex dynamics

Figure 14 illustrates the isosurfaces of λ_2 for vortex identification (Jeong and Hussain 1995) at $t = 22$, 136, and 699 ms. During the first 650 ms of the 1,000-ms cardiac cycle, the inlet valve (or the tricuspid valve), which is located on the right side of the figure, was open, and the RV model was in the filling phase. A vortex ring was formed shortly after the inlet valve opened, as shown in Fig. 14a. One side of the ring then interacted with the

Fig. 12 Difference in the normalized streamline length inside the RV model between simply interpolated, $L^*_{\mathbf{u}_{int}}$, and corrected velocity field, $L^*_{\mathbf{u}_{int}+\mathbf{u}_{corr}}$. 4,913 streamlines were generated for each studied field. Lengths were normalized by the longest streamline in the divergence-free field. The histogram indicates that the corrected velocity field has longer streamlines
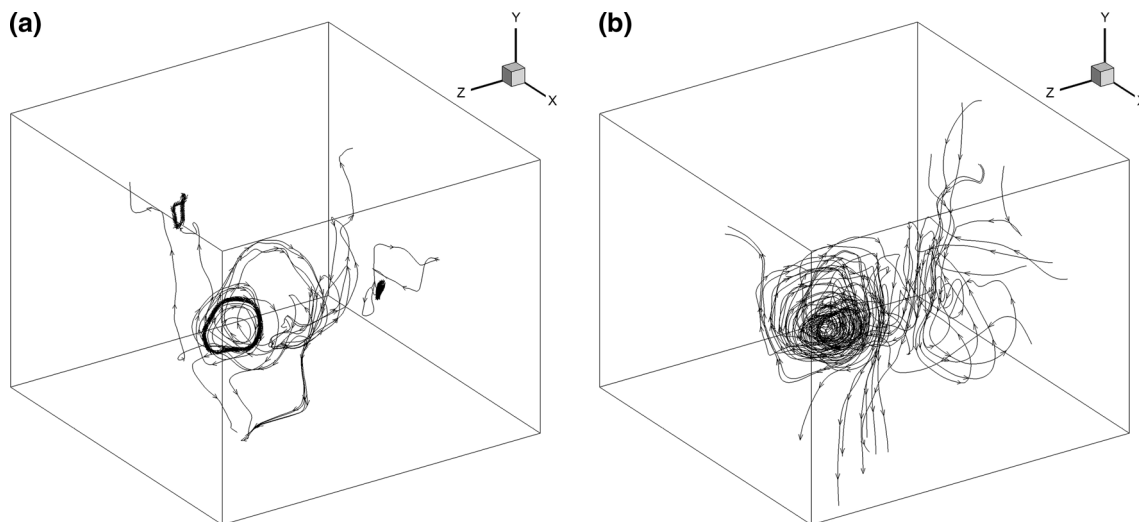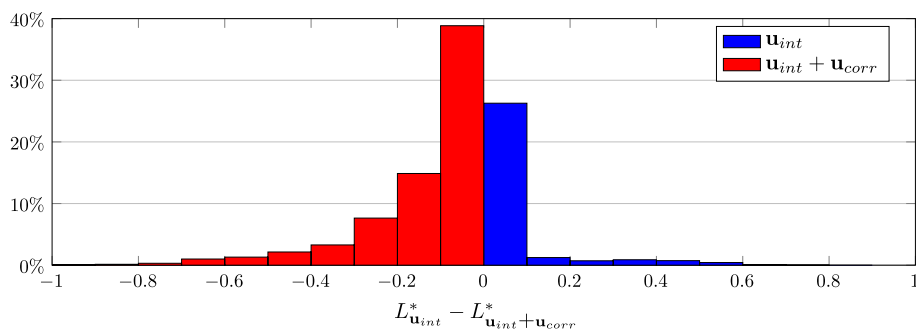

Fig. 13 Streamlines inside the RV model during the early diastole, $t = 30$ ms. **a** Some streamlines in the simply interpolated velocity field. **b** Streamlines originating at the same points for the divergence-free interpolated velocity field
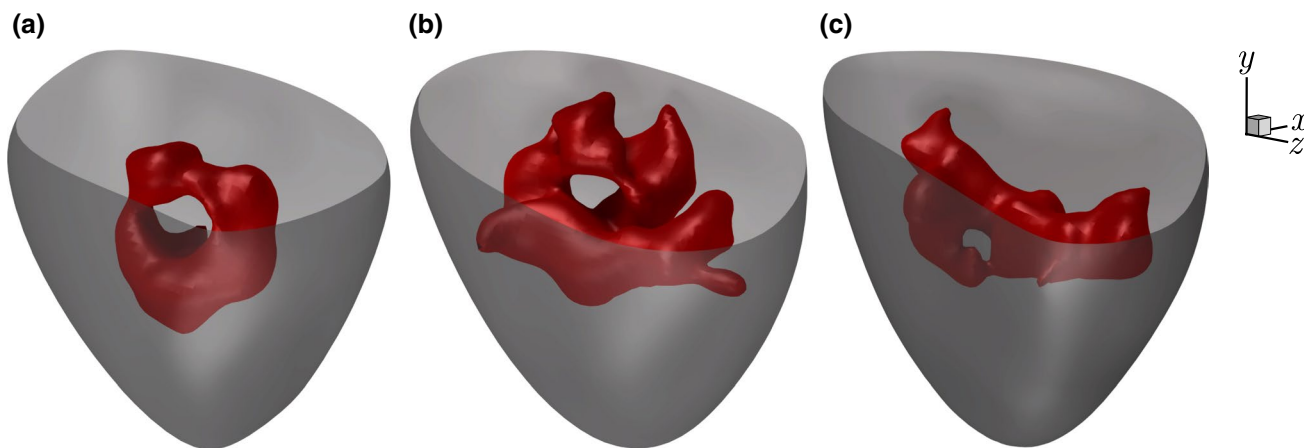

Fig. 14 Selected λ_2 isosurfaces of the flow inside the deforming RV chamber. **a** $\lambda_2 = -160\,\text{s}^{-2}$ at $t = 22$ ms; in **b**, $\lambda_2 = -40\,\text{s}^{-2}$ at $t = 136$ ms; **c** $\lambda_2 = -19\,\text{s}^{-2}$ at $t = 699$ ms

nearby wall and gave rise to an enhanced local dissipation that altered the vortex structure, as shown in Fig. 14b. At the end of the filling phase, the inlet valve closed and

the outlet valve, i.e., the pulmonary valve, opened for the next 350 ms of the cycle, pumping the fluid out of the RV model. In this phase, the vortex structure took the shape
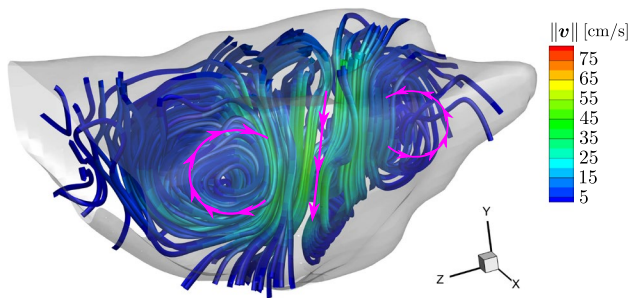
Fig. 15 3D divergence-free interpolated velocity field inside the RV model is shown during the early diastole, $t = 30$ ms. The boundary of the RV is shown in *light gray* for clarification. The streamlines, which are *colored* based on the velocity magnitude in cm/s, illustrate the jet and the vortex around it. The *pink arrows* overlaid on the streamlines schematically show the direction in which the fluid flows. The jet comes from the tricuspid valve during the filling (diastolic) phase

Fig. 16 Schematic of a 3D matrix ultrasound transducer. A matrix array ultrasound transducer can be used to simultaneously acquire images in multiple planes required by MPPIV. Using fewer ultrasound beams instead of the entire beams enables the transducer to complete scanning faster during a single heartbeat. These probes are currently used for performing 3D echocardiography of heart chambers. In the figure, the schematic of the multiple planes is shown

of a streamline filament elongating toward the exit, which corresponds to a helical motion along the converging outflow tract, as illustrated by Fig. 14c. Figure 15 shows the streamlines, including the jet and the vortex around it, in the early filling phase of the RV model. The RV wall was roughly obtained by image processing of its boundaries in different planes, as shown in Fig. 15 by gray isosurfaces. The unidirectional streamlines show the jet through tricuspid valve toward the apex of the RV model. It was observed that the trans-tricuspid jet is accompanied by a vortex structure that forms during the filling phase of the RV, which is shown by the rotational flows around the jet in Fig. 15.

5 Suitability of MPPIV for matrix array ultrasound transducers

MPPIV is developed as a general method for reconstructing a flow field in 3D based on multi-planar velocimetry. The advantage of this method when compared to the well-established 3D velocimetry techniques such as stereoscopic (Adrian 2005), defocusing (Pereira and Gharib 2002), or holographic PIV (Barnhart et al. 1994) lies in its compatibility to echocardiographic applications. The velocimetry techniques mentioned above require illumination of the flow by a light source(s). However, the current 3D echocardiography does not provide a framework to implement conventional PIV techniques with an acceptable temporal and spatial resolution. This is mainly due to the limited frame rate of 3D echocardiographic acquisitions, a limitation related to computational requirements of parallel processing of large datasets of ultrasound RF data in addition to the fixed speed of ultrasound waves that would require a substantial technological advancement to be overpassed.
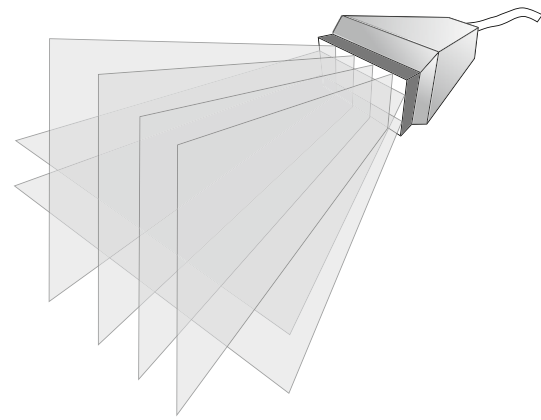
A recent advancement in ultrasound probe technology, i.e., matrix array probes, allows simultaneous and multi-plane recordings. Using this technology, 2D velocity data in multiple planes can be acquired simultaneously and recombined a posteriori to reconstruct a 3D velocity field. These echocardiographic systems employ matrix array ultrasound probes, and the substitution of full-volume scanning with multiple scan-planes (which can be done by activating fewer rows/columns on the same matrix probe, as shown in Fig. 16) would theoretically permit simultaneous multi-plane acquisitions. Therefore, a MPPIV solution would advance the development of imaging technologies for in vivo real-time 3D velocimetry with many applications such as cardiac imaging.

6 Limitations

From a methodological standpoint, the presence of the walls, as well as the different resolutions of in-slice and cross-slice data, may result in calculation of the divergence whose accuracy is either inhomogeneous (due to the presence of the wall) or non-isotropic (because of different resolutions along the different directions). These effects may influence the accuracy of the correction procedure. Refractive index matching was not used in 2C-PIV experiments for the RV model ($n_{water} = 1.333$, $n_{plexiglas} = 1.490$, $n_{siliconesac} = 1.336$). There was not much reflection at the interface of silicone model, and water as their refractive indices is comparable. However, the errors associated with optical distortion between Plexiglas and water still exist.

7 Conclusions

This work aimed to develop a method capable of improving the accuracy of flow fields obtained experimentally in 3D. The method employs 2C-PIV and constraints of incompressibility using a fractional step approach, in order to reconstruct a 3D flow field from multiple perpendicular 2D fields. This method can estimate the out-of-plane component of the velocity and results in a divergence-free 3D velocity field.

The method was validated using analytical, numerical, and experimental methods. Results revealed that by increasing the number of perpendicular planes, the RMS error was reduced. In addition, for a divergence-free field with no noise, correction improvement was small. We found that as the noise level in the flow field becomes larger, (i.e., resulting in a larger deviation of the divergence of the velocity from zero), the correction significantly improved the simply interpolated velocity fields. This procedure ensures a theoretical consistency that, besides the velocity field itself, may dramatically improve the calculations of quantities derived from velocity gradients, which intrinsically incorporate the zero-divergence condition.

References

Adrian RJ (2005) Twenty years of particle image velocimetry. Exp Fluids 39(2):159–169

Afanasyev Y, Demirov E (2005) A variational filtration and interpolation technique for PIV employing fluid dynamical constraints. Exp Fluids 39(5):828–835

Asakawa D, Pappas G, Blemker S, Drace JE, Delp S et al (2003) Cine phase-contrast magnetic resonance imaging as a tool for quantification of skeletal muscle motion. In: Seminars in musculoskeletal radiology, THIEME, vol 7, pp 287–296

Barnhart DH, Adrian RJ, Papen GC (1994) Phase-conjugate holographic system for high-resolution particle-image velocimetry. Appl Opt 33(30):7159–7170

Cimino S, Pedrizzetti G, Tonti G, Canali E, Petronilli V, De Luca L, Iacoboni C, Agati L (2012) In vivo analysis of intraventricular fluid dynamics in healthy hearts. Eur J Mech B Fluids 35:40–46

Cressie N (1992) Statistics for spatial data. Terra Nova 4(5):613–617

Domenichini F (2011) Three-dimensional impulsive vortex formation from slender orifices. J Fluid Mech 666:506–520

Falahatpisheh A, Kheradvar A (2012) High-speed particle image velocimetry to assess cardiac fluid dynamics in vitro: from performance to validation. Eur J Mech B Fluids 35:2–8

Fredriksson AG, Zajac J, Eriksson J, Dyverfeldt P, Bolger AF, Ebbers T, Carlhäll CJ (2011) 4-D blood flow in the human right ventricle. Am J Physiol Heart Circ Physiol 301(6):H2344–H2350

Gunes H, Rist U (2007) Spatial resolution enhancement/smoothing of stereo-particle-image-velocimetry data using proper-orthogonal-decomposition-based and Kriging interpolation methods. Phys Fluids 19(064):101

Gunes H, Rist U (2008) On the use of kriging for enhanced data reconstruction in a separated transitional flat-plate boundary layer. Phys Fluids 20(104):109

Harlander U, Wright GB, Egbers C (2012) Reconstruction of the 3D flow field in a differentially heated rotating annulus by synchronized particle image velocimetry and infrared thermography measurements. In: 16th International symposium on applied laser techniques to fluid mechanics, Lisbon, Portugal

Hill MJM (1894) On a spherical vortex. Proc R Soc Lond 55(331–335):219–224

Hong GR, Pedrizzetti G, Tonti G, Li P, Wei Z, Kim JK, Baweja A, Liu S, Chung N, Houle H et al (2008) Characterization and quantification of vortex flow in the human left ventricle by contrast echocardiography using vector particle image velocimetry. JACC Cardiovasc Imaging 1(6):705–717

Jeong J, Hussain F (1995) On the identification of a vortex. J Fluid Mech 285(69):69–94

Kheradvar A, Gharib M (2009) On mitral valve dynamics and its connection to early diastolic flow. Ann Biomed Eng 37(1):1–13

Kheradvar A, Houle H, Pedrizzetti G, Tonti G, Belcik T, Ashraf M, Lindner JR, Gharib M, Sahn D (2010) Echocardiographic particle image velocimetry: a novel technique for quantification of left ventricular blood vorticity pattern. J Am Soc Echocardiogr 23(1):86–94

Kim H, Hertzberg J, Shandas R (2004) Development and validation of echo PIV. Exp Fluids 36(3):455–462

Kim J, Moin P (1985) Application of a fractional-step method to incompressible Navier–Stokes equations. J Comput Phys 59(2):308–323

Leonard A (1985) Computing three-dimensional incompressible flows with vortex elements. Annu Rev Fluid Mech 17(1):523–559

Liburdy JA, Young EF (1992) Processing of three-dimensional particle tracking velocimetry data. Opt Lasers Eng 17(3):209–227

Mangual J, Domenichini F, Pedrizzetti G (2012) Three dimensional numerical assessment of the right ventricular flow using 4D echocardiography boundary data. Eur J Mech B Fluids 35:25–30

Mullin JA, Dahm WJ (2005) Dual-plane stereo particle image velocimetry (DSPIV) for measuring velocity gradient fields at intermediate and small scales of turbulent flows. Exp Fluids 38(2):185–196

Mullin JA, Dahm WJ (2006) Dual-plane stereo particle image velocimetry measurements of velocity gradient tensor fields in turbulent shear flow. I. Accuracy assessments. Phys Fluids 18(035):101

Norbury J (1973) A family of steady vortex rings. J Fluid Mech 57(3):417–431

Novikov E (1983) Generalized dynamics of three-dimensional vortical singularities (vortons). Zh Eksp Teor Fiz 84:981

Núñez MA, Flores C, Juárez H (2006) A study of hydrodynamic mass-consistent models. J Comput Methods Sci Eng 6(5):365–385

Núñez MA, Flores C, Juárez H (2007) Interpolation of hydrodynamic velocity data with the continuity equation. J Comput Methods Sci Eng 7(1):21–42

Pereira F, Gharib M (2002) Defocusing digital particle image velocimetry and the three-dimensional characterization of two-phase flows. Meas Sci Technol 13(5):683

Poelma C, Mari J, Foin N, Tang MX, Krams R, Caro C, Weinberg P, Westerweel J (2011) 3D flow reconstruction using ultrasound piv. Exp fluids 50(4):777–785

Ratto C, Festa R, Romeo C, Frumento O, Galluzzi M (1994) Mass-consistent models for wind fields over complex terrain: the state of the art. Environ Softw 9(4):247–268

Sengupta PP, Pedrizzetti G, Kilner PJ, Kheradvar A, Ebbers T, Tonti G, Fraser AG, Narula J (2012) Emerging trends in CV flow visualization. JACC Cardiovasc Imaging 5(3):305–316

Stamatopoulos C, Mathioulakis D, Papaharilaou Y, Katsamouris A (2011) Experimental unsteady flow study in a patient-specific abdominal aortic aneurysm model. Exp fluids 50(6):1695–1709

Su LK, Dahm WJ (1996) Scalar imaging velocimetry measurements of the velocity gradient tensor field in turbulent flows. I. Assessment of errors. Phys Fluids 8:1869–1882

Sung J, Yoo J (2001) Three-dimensional phase averaging of time-resolved piv measurement data. Meas Sci Technol 12(6):655

Vedula P, Adrian R (2005) Optimal solenoidal interpolation of turbulent vector fields: application to PTV and super-resolution PIV. Exp Fluids 39(2):213–221

Westerdale J, Belohlavek M, McMahon EM, Jiamsripong P, Heys JJ, Milano M (2011) Flow velocity vector fields by ultrasound particle imaging velocimetry in vitro comparison with optical flow velocimetry. J Ultrasound Med 30(2):187–195

Willert C, Gharib M (1991) Digital particle image velocimetry. Exp Fluids 10(4):181–193

Zhang F, Lanning C, Mazzaro L, Barker AJ, Gates PE, Strain WD, Fulford J, Gosling OE, Shore AC, Bellenger NG et al (2011) In vitro and preliminary in vivo validation of echo particle image velocimetry in carotid vascular imaging. Ultrasound Med Biol 37(3):450–464

Zhong J (1995) Vector-valued multidimensional signal processing and analysis in the context of fluid flows. PhD thesis, University of Illinois, Chicago

Zhong JL, Weng JY, Huang TS (1991) Vector field interpolation in fluid flow. In: Digital Signal. Processing '91, Int'l. Conf. on DSP, Florence, Italy

Ziskin I, Adrian R, Prestridge K (2011) Volume segmentation tomographic particle image velocimetry. In: Proceedings of 9th international symposium on particle image velocimetry. Kobe University, Kobe, Japan, pp 21–23